Journal of Materials Chemistry A

ROYAL SOCIETY OF CHEMISTRY

PAPER

View Article Online
View Journal | View Issue

Cite this: J. Mater. Chem. A, 2026, 14, 10822

Scalable fabrication of all-ceramic composite cathodes *via* controlled lithium compensation for Li-garnet batteries

Steffen Weinmann,[a] Marina Reis,[a] Michael Warnke,[a] Lucie Quincke,[a] Alena Gruendl,[b] Jennifer L. M. Rupp[acd] and Kun Joong Kim*[a]

Received 21st November 2025
Accepted 27th January 2026

DOI: 10.1039/d5ta09479h

rsc.li/materials-a

Developing scalable processing routes for oxide-based solid-state batteries remains a central challenge, particularly in maintaining lithium stoichiometry and interfacial stability during high-temperature sintering. In this work, we develop alternative lithium compensation strategies for the fabrication of fully dense, secondary-phase-free composite cathodes beyond gas-phase lithiation, using $LiCoO_2$–$Li_7La_3Zr_2O_{12}$ as a model system. Specifically, two solid-phase approaches were explored: the addition of lithium precursors and the use of an overlithiated garnet catholyte. Both methods effectively suppressed the formation of $LaCoO_3$-type interphases and yielded highly dense microstructures after sintering at 1050 °C, achieving performance comparable to gas-phase lithium compensation. These results, first verified on pellet samples, were successfully translated into flat, 100 μm-thick free-standing membranes *via* a tape casting process, demonstrating versatility and scalability. The membranes reduce the area-specific resistance to 4.5 Ω cm^2 while maintaining high electrochemical activity and delivering a discharge capacity of up to 1.49 mAh cm^{-2} at 0.25 mA cm^{-2}. These advances establish a scalable route toward industrially relevant, all-ceramic composite cathodes for garnet-based solid-state batteries.

Introduction

Lithium-ion batteries (LIBs) dominate energy storage across applications ranging from portable electronics to electric vehicles.[1] However, despite substantial progress, their reliance on flammable liquid electrolytes poses inherent safety risks, particularly under abuse conditions such as overcharging, mechanical impact, or elevated temperature.[2,3] In addition, LIBs continue to face challenges related to moderate energy density and limited fast-charging capability over a wide temperature range. These limitations have accelerated global efforts toward next-generation battery technologies with both enhanced performance and improved intrinsic safety.[4–6] Solid-state batteries (SSBs) have emerged as promising candidates for future energy storage due to their potential to offer higher energy densities, enhanced safety, and improved thermal and chemical stability, while simultaneously enabling lithium metal anodes.[5] Among the various solid electrolytes, Li-garnet-type lithium lanthanum zirconium oxide ($Li_7La_3Zr_2O_{12}$, LLZO) stands out as a leading oxide electrolyte.[2,7–9] LLZO exhibits high ionic conductivity (~10^{-3} S cm^{-1} at room temperature) with a wide electrochemical stability window and excellent compatibility toward lithium metal anodes.[3,10,11] These attributes have driven extensive research into LLZO-based SSBs, leading to major progress in understanding and mitigating the high interfacial resistance and lithium dendrite formation at the LLZO/lithium metal anode interface, particularly through advances in wetting layers, removing surface contamination, using mixed conducting interlayers, and optimizing anolyte microstructure.[12–18] On the other hand, progress on the cathode side – typically designed as an all-ceramic composite with a solid electrolyte – remains comparatively slow, constrained by the limited choice of chemically compatible active materials and their inherent instability during high-temperature fabrication. These challenges often result in high interfacial resistance between LLZO and conventional cathode active materials such as $LiCoO_2$ (LCO), layered $LiN_xMn_yCo_zO_2$ (NMC) oxides, and $LiFePO_4$.[19–21] This leads to the formation of electrochemically inactive, highly resistive secondary phases such as $LaCoO_3$ and $LiLa_4CoO_8$.[20,22,23]

Several mitigating strategies have been investigated, including low-temperature sintering,[24] radiation-assisted densification,[21,22,25] and lithium-rich co-firing atmospheres.[5,23,26,27] In our previous work, we demonstrated that employing a Li_2O-rich atmosphere during co-firing of LCO-

[a]Technical University of Munich, TUM School of Natural Sciences, Department of Chemistry, Chair for Solid-State Electrolytes, Lichtenbergstraße 4, 85748 Garching, Germany. E-mail: kunjoong.kim@tum.de

[b]Technical University of Munich, TUM School of Engineering and Design, Department of Mechanical Engineering, Institute for Machine Tools and Industrial Management, Boltzmannstrasse 15, 85748 Garching, Germany

[c]TUMint. Energy Research GmbH, Lichtenbergstraße 4, 85747 Garching, Germany

[d]Fritz-Haber-Institute of the Max-Planck-Society, Faradayweg 4-6, 14195 Berlin, Germany

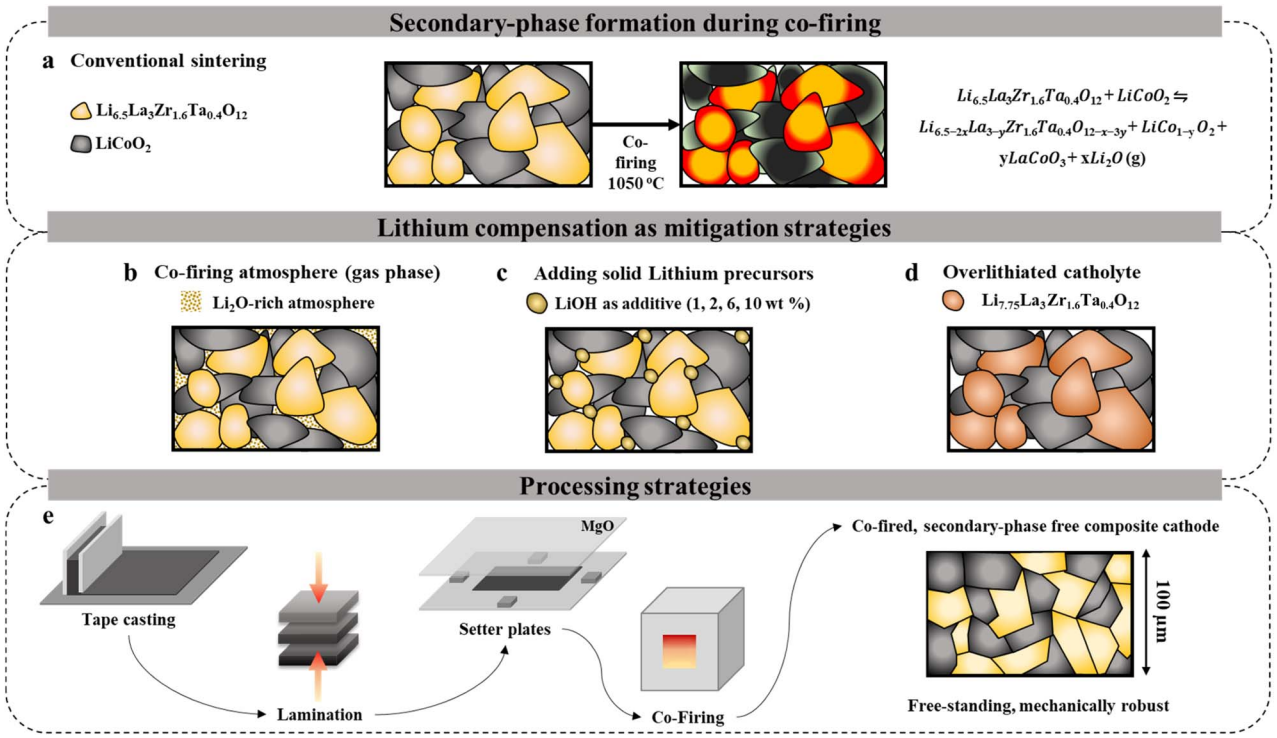

Fig. 1 Overview of co-firing strategies to produce all-ceramic LLZO-LCO composite cathodes. (a) Conventional co-firing at 1050 °C results in secondary phase formation, $LaCoO_3$, on the LLZO grains. (b) Gas-phase lithium compensation. Alternative solid-state lithium compensation *via* (c) LiOH addition and (d) Overlithiated LLZO within cathode. (e) Scalable process using tape casting, lamination and co-firing used in this work for a ~100-micron-thick free-standing composite cathode membrane.

LLZO composite cathodes is an effective approach to suppressing secondary phase formation.[23] This method compensates for lithium volatilization from LLZO, which otherwise can trigger a cascade of reactions, due to partial decomposition of LLZO into La_2O_3 and subsequent Co^{3+} cross-diffusion (Fig. 1a). By sustaining a Li_2O-rich atmosphere during firing, the elevated Li_2O vapor pressure shifts the defect equilibrium, suppressing lithium and oxygen vacancy formation and thereby preventing the decomposition and the formation of $LaCoO_3$-type interphase. Under these conditions, the formation of the interphase was effectively suppressed, resulting in fully-dense (*i.e.* $\rho_{relative} \approx 96.5\%$) composite cathodes with high specific capacity and markedly reduced area-specific resistance (Fig. 1b).[23] However, the firing approach based on vapor-phase lithium compensation in a semi-closed crucible, while scientifically effective, poses practical challenges for scalability, precise atmosphere control, and uniform lithium supply.

Herein, we develop scalable routes to sustain high Li_2O vapor pressure during the firing of LLZO-LCO composite cathodes. Specifically, a gas-phase lithium compensation method is compared with a solid-phase route, where a small fraction of LiOH is incorporated into the composite cathode prior to firing (Fig. 1c). Additionally, a lithium-rich garnet phase of 7.75 Li per formula unit (pfu) (*i.e.*, $Li_{7.75}La_3Zr_{1.6}Ta_{0.4}O_{12}$) is employed as an overlithiated electrolyte within the cathode to compensate for lithium loss during the firing process (Fig. 1d). Finally, the developed lithium compensation strategies are implemented in a high-throughput and continuous tape casting process to fabricate mechanically robust, free-standing composite cathodes with industrially relevant form factors (Fig. 1e). The process produces dense, secondary-phase-free, ~100 μm-thick free-standing all-ceramic composite cathode membranes that exhibit low area-specific resistance with a high utilization of active materials during initial cycles. By clarifying how lithium loss drives secondary-phase formation and by providing practical compensation windows, this work opens a scalable and more sustainable manufacturing route for oxide SSB components. Critically, it also lays the groundwork for fabricating cathode half-cell and full-cell prototypes through a single-step co-firing process, which minimizes energy consumption and cost by eliminating multiple high-temperature firing steps.[6,28]

Results

Sintering behavior

A series of composite cathodes consisting of LCO and LLZO with three different lithiation strategies during synthesis and processing were examined (Table 1). In the following, the different composite cathodes are referred to as LCO-$LLZO_{atm}$ *via* atmospheric compensation, LCO-$LLZO_{add}$ *via* LiOH addition, and LCO-$LLZO_{ov}$ *via* overlithiation of the LLZO catholyte.

The pristine composite cathode shows a yellow–grey appearance (Fig. 2a inset) and low relative density of 86 ± 3% due to the second phase formation of $LaCoO_3$.[23] Cross-sectional scanning electron microscopy (SEM) images show a highly porous microstructure with limited neck growth between the

Table 1 Summary of relative density, grain size of LCO and LLZO, and fabrication conditions for each composite cathode of LCO-LLZO. As a baseline, all samples were sintered at 1050 °C for 2 h under flowing oxygen in a closed-lid crucible using mother powder. LLZO powders used in pristine, LCO-LLZO$_{atm}$ and LCO-LLZO$_{add}$ were synthesized with 15 wt% excess LiOH during calcination. The overstoichiometric LLZO powder for LCO-LLZO$_{ov}$ was synthesized with a higher target Li content (7.75 pfu) without external additives. *$Li_{7.75}La_3Zr_{1.6}Ta_{0.4}O_{12}$

Sample	Density [%]	LCO grain size [μm]	LLZO grain size [μm]	Target Li in LLZO [pfu]	Firing condition
Pristine	86 ± 3	3.5 ± 3.2	1.6 ± 0.8	6.45	Baseline firing only
LCO-LLZO$_{atm}$	96 ± 2	4.8 ± 2.0	2.2 ± 2.5	6.45	LiOH bed powder for Li-rich atmosphere
LCO-LLZO$_{add}$	94 ± 2	4.1 ± 2.3	1.9 ± 0.3	6.45	1 wt% LiOH added as additive
LCO-LLZO$_{ov}$	95 ± 2	4.4 ± 2.9	1.6 ± 1.2	7.75*	Baseline firing only

LLZO–LLZO, LCO–LCO and LLZO–LCO interfaces (Fig. 2a, SI 1). The grain sizes of LLZO and LCO are around 1.6 ± 0.8 μm and 3.5 ± 3.2 μm, respectively. In contrast, all other composite cathodes show a uniform grey–black color and increased relative densities of 94–96%, and grain sizes of LLZO and LCO of 1.6–2.2 μm and 4.1–4.8 μm, respectively. Fractured surfaces of the LCO-LLZO$_{atm}$ and LCO-LLZO$_{ov}$ show intimate contact between LCO and LLZO grains without closed pores (SI 2) while the LCO-LLZO$_{add}$ shows some closed pores, likely caused by LiOH additive decomposition (1 wt%) and water outgassing.[29,30] A larger fraction of pores with hundreds-of-micrometers in diameter were observed in pellets with 2, 6, and 10 wt% additive

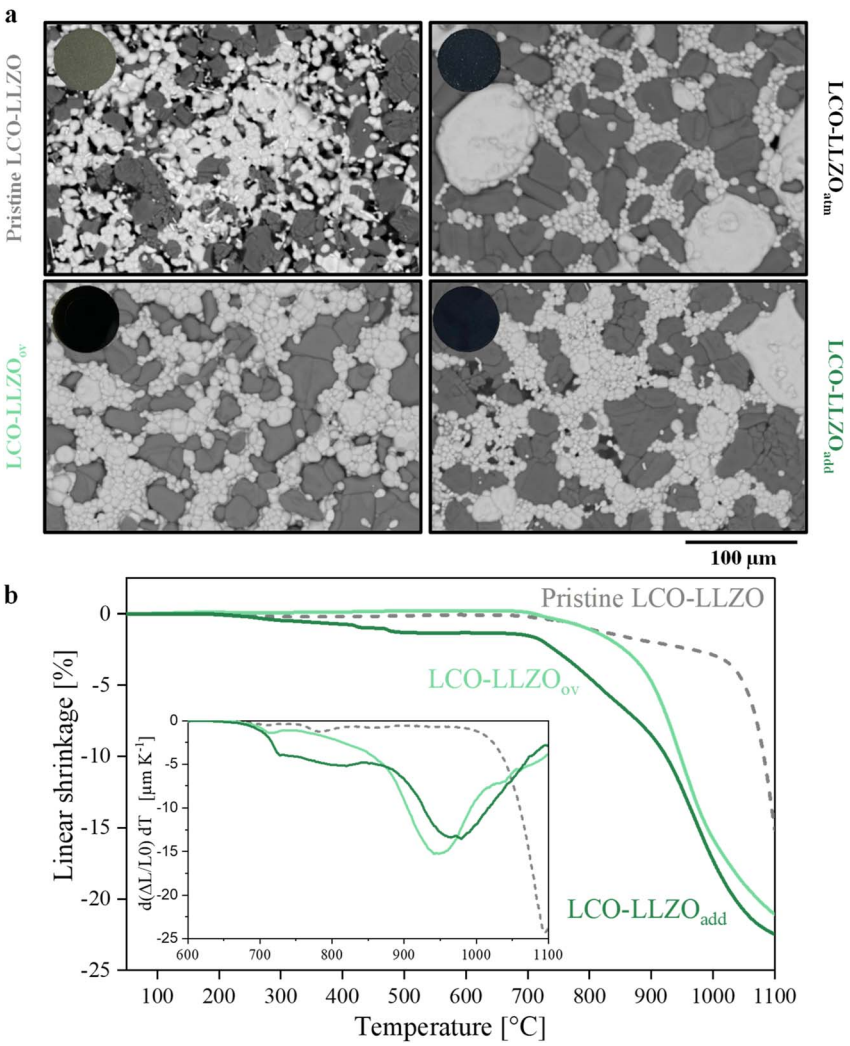

Fig. 2 Changes in microstructure and shrinkage for LCO-LLZO composite cathode. (a) SEM images of pristine, LCO-LLZO$_{atm}$, LCO-LLZO$_{add}$, LCO-LLZO$_{ov}$ after thermal etching alongside a picture of the samples (insets). (b) Shrinkage curves and their derivatives of pristine, LCO-LLZO$_{add}$ and LCO-LLZO$_{ov}$.

(SI 3) and further decreased relative density of 89%, 85%, and 81%, respectively. Overall, our results confirm that the selected lithium compensation strategies, particularly the addition of solid lithium precursors and the use of overlithiated LLZO, both promote the sintering of LCO-LLZO composite cathodes. This effect is consistent with the improvements observed when lithium is compensated *via* a gas-phase approach.

To elucidate the sintering behavior, Fig. 2b shows the dilatometry curves as shrinkage ($\Delta L/L_0$) and their first derivatives, $d(\Delta L/L_0)\,dT$ (inset), for three composite cathodes: Pristine, LCO-$LLZO_{add}$, and LCO-$LLZO_{ov}$. Due to limitations of the dilatometry setup, a lithium-rich atmosphere could not be established; consequently, no data are available for the LLZO-LCO_{atm} sample. All the tested samples exhibit only linear thermal expansion up to approximately 400 °C. At ≈400 °C, LCO-$LLZO_{add}$ enters an early densification regime, shrinking by about 1.5% as molten LiOH and any residual Li_2CO_3 presumably flood interparticle pores and enable particle rearrangement. The pristine sample remains largely inert until ≈1040 °C, reaches its maximum densification rate at ≈1090 °C, and accumulates a total ΔL of – 15% by 1100 °C. In contrast, both the LCO-$LLZO_{add}$ and LCO-$LLZO_{ov}$ composites begin densifying at a lower temperature of ≈720 °C and surpass 15% shrinkage by 1000 °C; the former reaches a total shrinkage of – 22.5%, while the latter attains – 21.5% at 1100 °C. The sintering onset for both samples starts slightly above 900 °C and reaches maximum densification rates between 945 °C and 975 °C. Overall, the more pronounced sintering behavior – both in the onset of densification and in the peak sintering rate – occurs about 100 °C below the pristine sample. Additionally, the derivative curve for LCO-$LLZO_{ov}$ is noticeably steeper than that of the LCO-$LLZO_{add}$, indicating more vigorous sintering driven by additional Li-rich vapor species outgassing from the overlithiated LLZO. This observation is consistent with ICP-OES measurements discussed later.

Phase characterization, lithium contents and chemical stability

Raman spectroscopy and X-ray diffraction (XRD) were used to identify the phases of the LLZO grains, LCO grains and their interfaces (Fig. 3). As-synthesized LLZO and commercial LCO serve as references (SI 4). In the averaged Raman spectra of pristine composite cathodes, all characteristic peaks of cubic-phase Ta-doped LLZO are present at 120, 210, 250, 360, 420, 640, and 730 cm^{-1} (E_g for La, T_{2g} and A_{1g} for O, T_{2g}, and E_g for Li, A_{1g} for Zr and A_{1g} for Ta modes, respectively).[31–33] LCO exhibits its characteristic bands at 485 cm^{-1} (E_g O–Co–O bending) and 595 cm^{-1} (A_{1g} O–Co–O stretching).[34] Notably, an additional peak appears at 685 cm^{-1}, attributed to $LaCoO_3$ (Fig. 3a)[23] and phase mapping confirms this second phase within the LLZO grains (Fig. 3b). By contrast, other composite cathodes yield Raman maps with sharply delineated LLZO and LCO regions and neither detectable $LaCoO_3$ phase nor from other impurities. The corresponding average spectra reveal only LLZO and LCO peaks, demonstrating complete suppression of the secondary phase formation. The intensity of the LLZO signals in the pristine sample is lower compared to the other samples, indicating the shadowing of the LLZO signal by the secondary phase. Additionally, XRD reveals only phase-pure LLZO and LCO in the lithium-compensated composite cathodes, whereas the pristine composite shows an additional signal attributed to rhombohedral $LaCoO_3$ (Fig. 3c).

To clarify how overlithiated LLZO (target Li content of 7.75 pfu) suppresses secondary phase formation during the composite cathode sintering process, its influence on phase

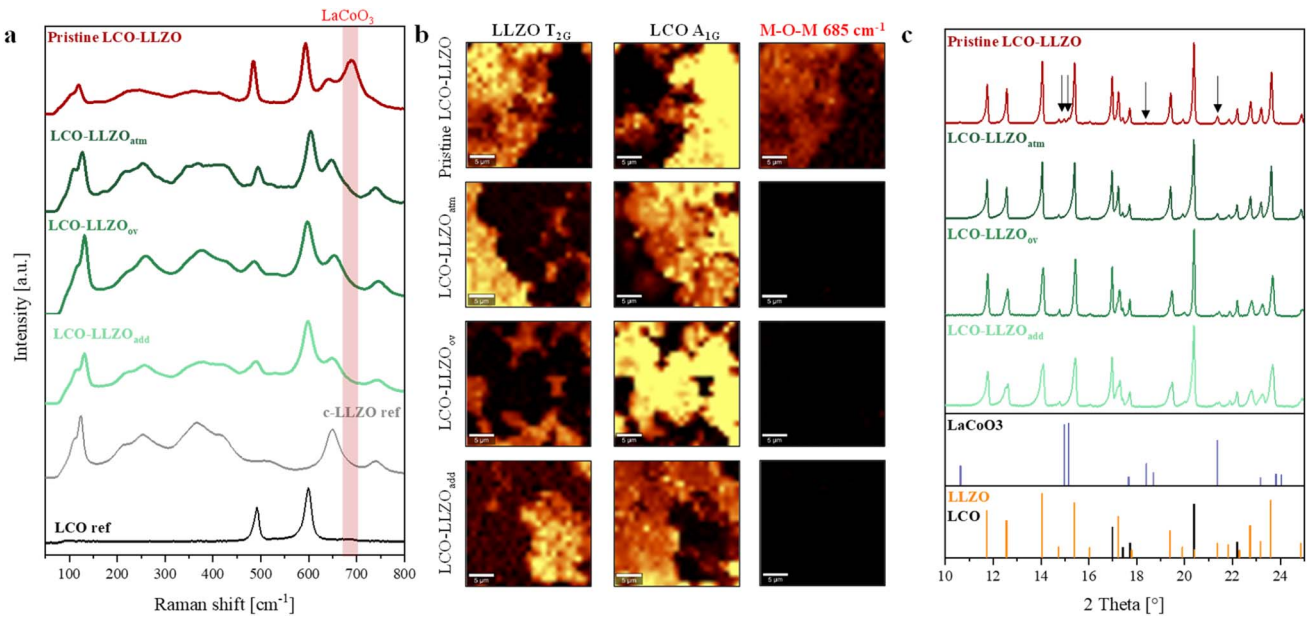

Fig. 3 (a) Raman spectroscopy mapping of LLZO/LCO interfaces with wavelength-filters for lithium-compensated and pristine samples in a 25 × 25 μm area. (b) Average Raman spectra for the LCO-LLZO co-fired cathodes from the mapped area. (c) p-XRD measurements of the samples.

evolution (SI 5) and lattice parameters (SI 6) were examined. As-synthesized $LLZO_{ov}$ powder shows slight peak splitting at $2\theta = 30.5°$ in the XRD patterns,[35] together with a subtle shoulder in the Li–O_6 Raman band, indicates incipient symmetry lowering, *e.g.* through tetragonal distortion. Excess Li can occupy additional octahedral sites, modifying the local bonding environment and lattice vibrations. Beyond a critical Li content, the resulting Li–Li repulsion destabilizes the cubic structure and drives its transformation to the tetragonal phase.[36] Additionally, the lattice parameter increased to 12.951 Å compared to pristine LLZO (12.948 Å, SI 6), indicating that excess Li ions likely occupy sites near oxygen anions, thereby enhancing Li–Li repulsion. Nonetheless, after overlithiated LLZO inside the cathode was exposed to 1050 °C for 2 h during firing, its structure reverted to the cubic phase (Fig. 3a), and the lattice parameter decreased back to ~12.947 Å, like that of pristine LLZO. This behavior is likely due to the lithium content dropping below the stability threshold of the cubic phase. The lost lithium may also influence the nearby LCO structure, as reflected in the different lattice parameters change observed after firing. In pristine LCO-LLZO, the LCO *c* parameter increased to 14.071 Å. As proposed in our previous studies, the expansion of the LCO *c* parameter in pristine samples originate from lithium loss.[23,37] This counter-intuitive expansion arises because Li vacancies increase the repulsive interactions between the CoO_2 layers, thereby widening the interlayer spacing.[38] In contrast, the *c*-axis lattice parameters of the as-sintered LCO-$LLZO_{ov}$ sample does not exhibit such increase but instead shows a slight decrease to 14.045 Å (SI 6), indicating a stabilizing effect on the layered structure. The stabilization can tentatively ascribed to two factors: (i) Overlithiated LLZO in LCO-$LLZO_{ov}$ counteracts the expansion associated with lithium-deficient interlayer spacing in LCO,[38] and (ii) Al^{3+} diffusion from LLZO into LCO contributes to lattice compression.[39]

Up to this point, all three lithium-loss compensation strategies for LCO-LLZO composite cathodes have been systematically tested and refined using pellet samples. However, since the transition from 700 μm-thick pellets to 100 μm-thick membranes entails a drastic change in sample geometry, it is important to understand how this factor can influence lithium evaporation and, consequently, secondary phase formation. To address this, we compared the lithium contents of LLZO samples – powder, pellet and tape – with and without applied compensation strategies through inductively coupled plasma optical emission spectroscopy (ICP-OES). Since Li-loss inside the LLZO is the driving force for secondary phase formation, we examined pure LLZO samples (Fig. 4a). Initially, as-synthesized, pristine LLZO powders exhibited stoichiometric lithium levels of around 6.77 pfu. Here, Li pfu denotes the total lithium content after dissolution and normalization. It should therefore not be interpreted as the lithium contents incorporated exclusively within the LLZO lattice, since minor Li-containing surface species or secondary species (*e.g.*, Li_2CO_3) may also contribute. Electrically, charge neutrality of the garnet phase is maintained through native point defects (primarily Li vacancies together with oxygen-related defects), rather than through changes in cation valence.[40] After firing at 1050 °C for 2 hours, lithium contents decreased by 0.22 pfu in the pellets and by 0.40 pfu in the tapes. This more than twofold increase in lithium loss between the pellets to tapes highlights the critical influence of sample geometry. Notably, the surface-to-volume ratio plays a decisive role. Tapes exhibit an approximately tenfold higher surface-to-volume ratio compared to pellets, placing a significantly larger fraction of lithium atoms in proximity to the surface. Since lithium evaporates from the surface and diffusion paths are shorter to replenish near-surface lithium, the overall loss becomes more pronounced in tapes.[41] Moreover, the decomposition of organic components during the debinding

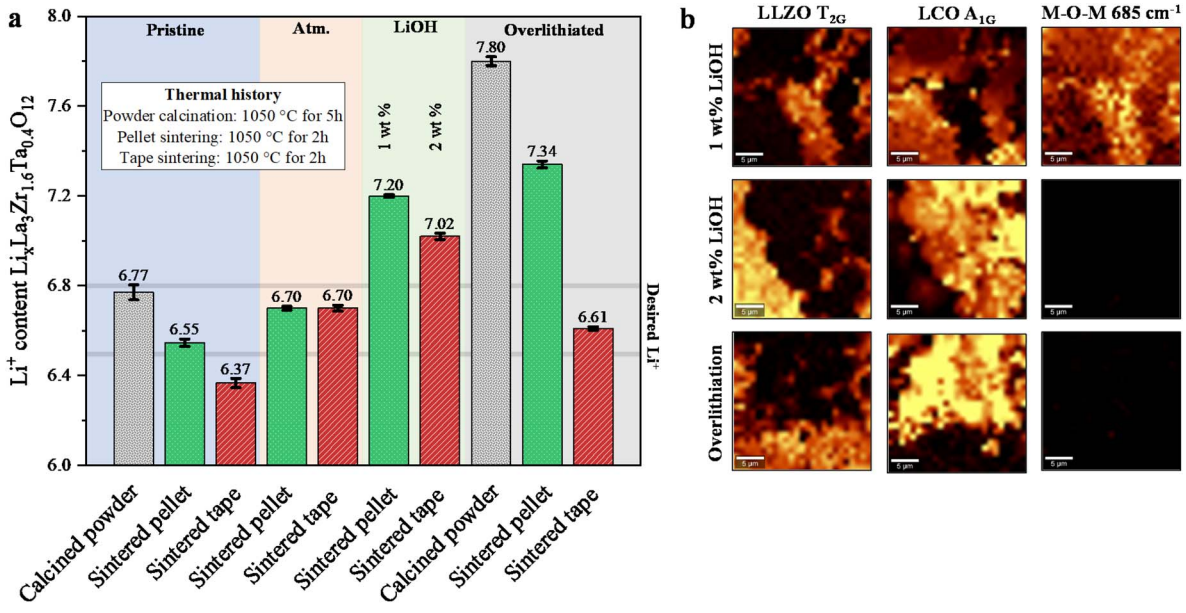

Fig. 4 (a) ICP-OES results for the Li^+ content in LLZO powders, pellets and tapes processed in Li-rich atmosphere, with LiOH additives or with overlithiated powders. (b) Filtered Raman maps for tapes made with 1 wt% and 2 wt% LiOH as well as overlithiated LLZO powders.

process of tapes at low temperature results in increased porosity, enhancing the surface area exposed at elevated temperature. Since lithium depletion contributes to secondary phase formation when combined with LCO cathodes, it is crucial to account for such effects in processing strategies. Understanding and mitigating lithium loss is therefore essential, not only for maintaining the structural integrity of LLZO but also for preventing undesirable reactions and secondary phase formation at the cathode–electrolyte interface.

When examining LLZO pellets and tapes processed in a Li_2O-rich atmosphere, it was observed that, within experimental errors, there was no significant lithium loss. This supports the hypothesis that such an atmosphere suppresses lithium evaporation by shifting the chemical potential of Li_2O, thereby reducing the driving forces for lithium outgassing.

For the additive method, to compensate for the 0.22 pfu lithium lost during pellet firing relative to the pristine powder, we estimated that at least 0.6 wt% LiOH are required. This value is derived from molar ratio between lithium in LiOH and the total lithium content in LLZO (*i.e.* $Li_{6.77}La_3Zr_{1.6}Ta_{0.4}O_{12}$), assuming complete decomposition of LiOH to Li_2O during firing. The resulting Li_2O vapor equilibrates with the LLZO surface, supplying Li and oxygen ions. Lithium incorporation is therefore considered to occur through surface reaction and subsequent bulk diffusion of Li^+ under a sustained Li_2O vapor pressure. Consequently, 1 wt% LiOH suffices to compensate for lithium loss in pellets (Fig. 3) but is inadequate for tapes, as evidenced by secondary phase formation (Fig. 4b). This inadequacy arises from the significantly higher surface-to-volume ratio of tapes, which accelerates lithium evaporation and requires more excess lithium in LLZO tape. Therefore, 2 wt% LiOH were chosen for tapes, resulting in no detectable impurities in Raman analysis. Comparing the 1 wt% LiOH added pellet and 2 wt% LiOH added tapes after firing, the measured lithium contents were 7.2 and 7.02 pfu, respectively, indicating that the added amounts may have been overestimated and can be adjusted to achieve optimal lithium stoichiometry. Nonetheless, the 2 wt% LiOH added tapes yield secondary phase-free composite cathode tapes (Fig. 4b). Furthermore, Li_2CO_3 and Li_2O were evaluated as alternative lithium-compensating additives in a pellet-based composite cathodes. Stoichiometric calculation indicates that at least 0.4 wt% Li_2O and 1 wt% Li_2CO_3 are required for lithium compensation. Experimentally, both LiOH and Li_2O at 1 wt% yield secondary phase-free composite cathode, whereas at least 2 wt% Li_2CO_3 is necessary (SI 7). Since LiOH decomposes to Li_2O and H_2O upon heat treatment,[29] comparable results for LiOH and Li_2O are expected. Finally, overlithiated LLZO powders, pellets, and tapes are examined. To counterbalance the lithium loss, synthesis targeted 7.75 pfu Li, which is confirmed to be 7.8 (Fig. 4a). The lithium loss was approximately 5.9% for pellets and 15.3% for tapes after firing, indicating a higher lithium evaporation rate compared to the pristine LLZO, likely due to the higher initial lithium chemical potential and partial surface segregation of lithium species. Nonetheless, the tapes still achieved a cubic LLZO (Fig. 4b), free of second phases, while maintaining the initially targeted lithium content of around 6.61 pfu Li. For Ta-doped LLZO, the cubic phase with highest room-temperature ionic conductivity is typically obtained at Li contents of about 6.5 to 6.8 Li pfu; too few or too many Li^+ vacancies promote tetragonal ordering and inhibit optimal ionic transport pathways.[42,43]

Overall, both the tailored amount of LiOH additives and the use of overlithiated LLZO for LCO-LLZO composite cathodes effectively suppress the formation of secondary-phase $LaCoO_3$ in both pellet and tape samples (Fig. 4b, SI 8). For the LCO-$LLZO_{ov}$ samples, two mechanisms may explain the enhanced sintering behavior relative to pristine samples. First, lithium may be partially incorporated into the garnet lattice, which can induce a transient tetragonal distortion. Because lithium volatilizes uniformly from nanoscale particles, this establishes a locally lithium-rich atmosphere that accelerates sintering while preserving sufficient lithium to stabilize the cubic garnet phase and prevent decomposition into La_2O_3 or $La_2Zr_2O_7$. Second, a fraction of the additional lithium may remain outside the garnet lattice, existing as a thin surface coating or as minor phases such as Li_2O, LiOH, or Li_2CO_3, which can act as transient sintering aids during densification.

Mechanical integrity

When transitioning ceramic processing from 1 mm-thick pellets to 100 μm-thick sheet-type free-standing membranes for practical battery cell manufacturing, ensuring flatness and mechanical integrity of sintered membranes becomes critical. To address these challenges, ceramic setter plates were employed during the firing process. However, this approach introduces additional processing complexities. First, during the debinding process, the system must allow efficient outgassing of decomposition products from the organic binders in the green tape. If the gas release is hindered by the setter plate, it can lead to tape deformation, internal gas buildup, carbon residue, warping, and uneven sintering. Second, adhesion between the green tape and the setter plate must be avoided. If the tape sticks during sintering, it can lead to surface tearing, constrained shrinkage, and nonuniform densification. Polished MgO setter plates were found to be highly effective in this regard. At the applied firing temperature, MgO remains chemically inert toward the composite cathode and prevent bonding between the tape and the setter, likely due to its chemical inertness and negligible Mg^{2+} diffusion into LCO-LLZO composite.[44] In contrast, alumina setter plates caused severe sticking and even partial sintering between tape and setter (SI 9). This arises from the lithophilic nature of alumina, which reacts with lithium to form Li–Al–O compounds and draws lithium from LLZO and LCO, thereby promoting eutectic liquid formation, exacerbating lithium loss and promoting secondary phase formation.[45,46] These insights underscore that, in addition to the atmosphere and additive control, the setter plate selection plays a crucial role in achieving desired lithium stoichiometry and flatness during firing process. As illustrated in Fig. 1e, the green tape is placed on the setter plate, with a second setter plate positioned on top to act as warping restriction. Additionally, thin MgO spacers are placed between

the setter plates to facilitate the outgassing of decomposition products, minimize direct chemical interactions or sticking between the specimen and the setter plates, and allow more uniform access of the reactive atmosphere to the sample surface. These spacers are only a few microns thicker than the green tape and serve to limit tape warping during firing by providing localized support without imposing constant pressure across the entire tape surface. Using this setup, SEM analysis revealed that as-sintered tapes exhibit a dense and uniform microstructure (Fig. 5a). Notably, LCO-LLZO$_{add}$ displayed a slightly higher porosity and presence of larger pores (10–25 μm) (SI 10), attributed to the decomposition of LiOH particles during firing. These observations are concomitant with the microstructure observed in the pellets (Fig. 2a). As-sintered composite cathodes have a thickness of around 120–140 μm. As shown in the video (SI Video), the sample demonstrated good mechanical robustness, withstanding handling with tweezers and even accidently dropping without cracking. Although the sample shown in the video is LCO-LLZO$_{add}$, all three sample types demonstrated comparable mechanical behavior.

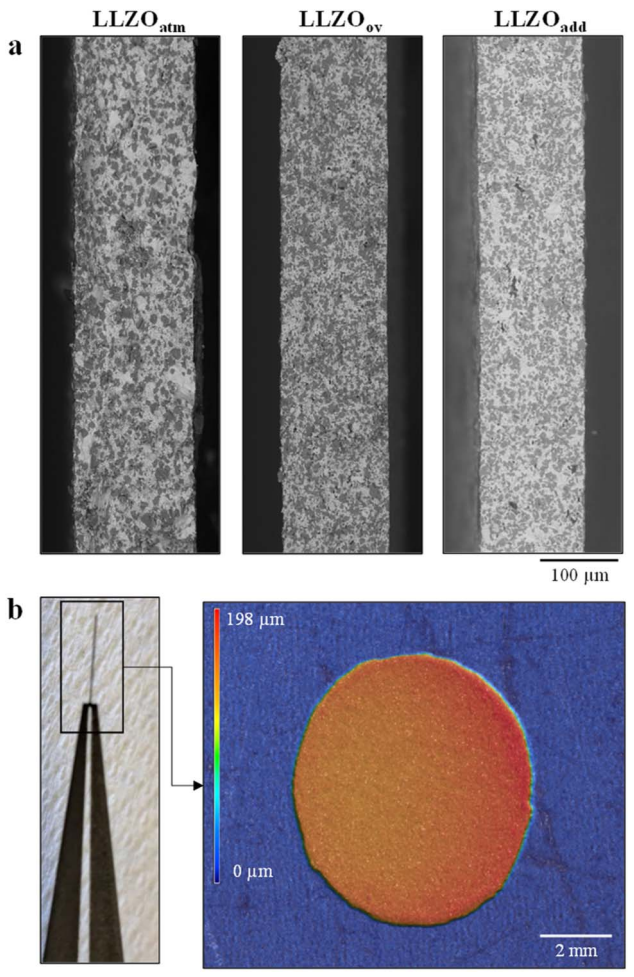

Fig. 5 (a) LLZO-LCO composite cathode sintered in Li_2O atmosphere (left), using overlithiated LLZO powder (middle), and 2 wt% LiOH additives (right). (b) 3D profilometry measurement of a flat LCO-LLZO$_{ov}$ cathode manufactured with the setter/spacer method.

3D profilometry confirmed that the composite cathode sheets are not only thin and flat (Fig. 5b) but also exhibit minimal surface roughness, with an areal surface roughness S_a of 9 μm. The S_a value, defined as the arithmetic mean of the absolute height deviations from the mean plane, is a standard metric for quantifying surface texture. In this case, the low S_a indicates excellent macroscopic flatness and minimal surface waviness. This is essential for maintaining even pressure distribution in a battery and avoiding interfacial gaps or pressure spikes that could damage the cathode during assembly or operation. The use of setter plates with spacers proved crucial in achieving such flatness, underscoring the importance of the firing setup in the tape casting process.

Electrochemical characterization

Because the LCO-LLZO composite behaves as a mixed conductor with predominantly electronic transport, DC chronoamperometry was used to determine its electronic conductivity (Fig. 6a). The three free-standing membranes exhibited electronic conductivities of ≈2.1–2.3 mS cm^{-1}, slightly lower than the pellet samples (3.15 mS cm^{-1}).[23] The reduced conductivity is likely attributable to microstructural differences (*e.g.*, residual porosity). Nevertheless, the reduced thickness (≈100 μm *vs.* ≈700 μm for the pellets) produces a substantially decreased total resistance of 4.5 Ω cm^2 for the membranes, compared with area specific resistance (ASR) ≈22.2 Ω cm^2 for the pellets[23] – an approximately fivefold reduction. Given typical cell component resistances, the electronic contribution to ASR is not expected to be the limiting factor in cell operation. To further elucidate the minor ionic contribution in the LCO-LLZO composite, potentiostatic electrochemical impedance spectroscopy (PEIS) measurements were performed with poly (ethylene oxide) (PEO) using a symmetric Steel|PEO|composite cathode|PEO|Steel configuration, designed to selectively probe Li^+ transport through the polymeric interlayer. However, this setup lacks a well-defined lithium chemical potential at the electrode interfaces, since both outer steel electrodes are blocking for Li^+ and the PEO layer cannot function as a true lithium reservoir. Consequently, the ionic flux across the cell cannot be sustained under either AC or DC perturbation, and the recorded response is dominated by interfacial polarization rather than steady-state ionic conduction. The apparent ionic conductivities derived from this configuration were therefore higher than expected (SI 11), likely reflecting capacitive artifacts and local polarization within the PEO–composite interfaces rather than intrinsic bulk transport. To achieve a physically meaningful separation between ionic and electronic conductivities, at least one non-blocking lithium reservoir electrode (*e.g.*, Li metal) must be employed to define the electrochemical potential of lithium and establish well-controlled boundary conditions, as described in the classical Hebb–Wagner framework.[47] The use of this approach for Li-oxide MIECs is, however, experimentally challenging because direct contact between Li metal and oxide composites often induces parasitic reduction reactions and interphase formation, leading to an unstable lithium chemical potential and unreliable steady-state currents.

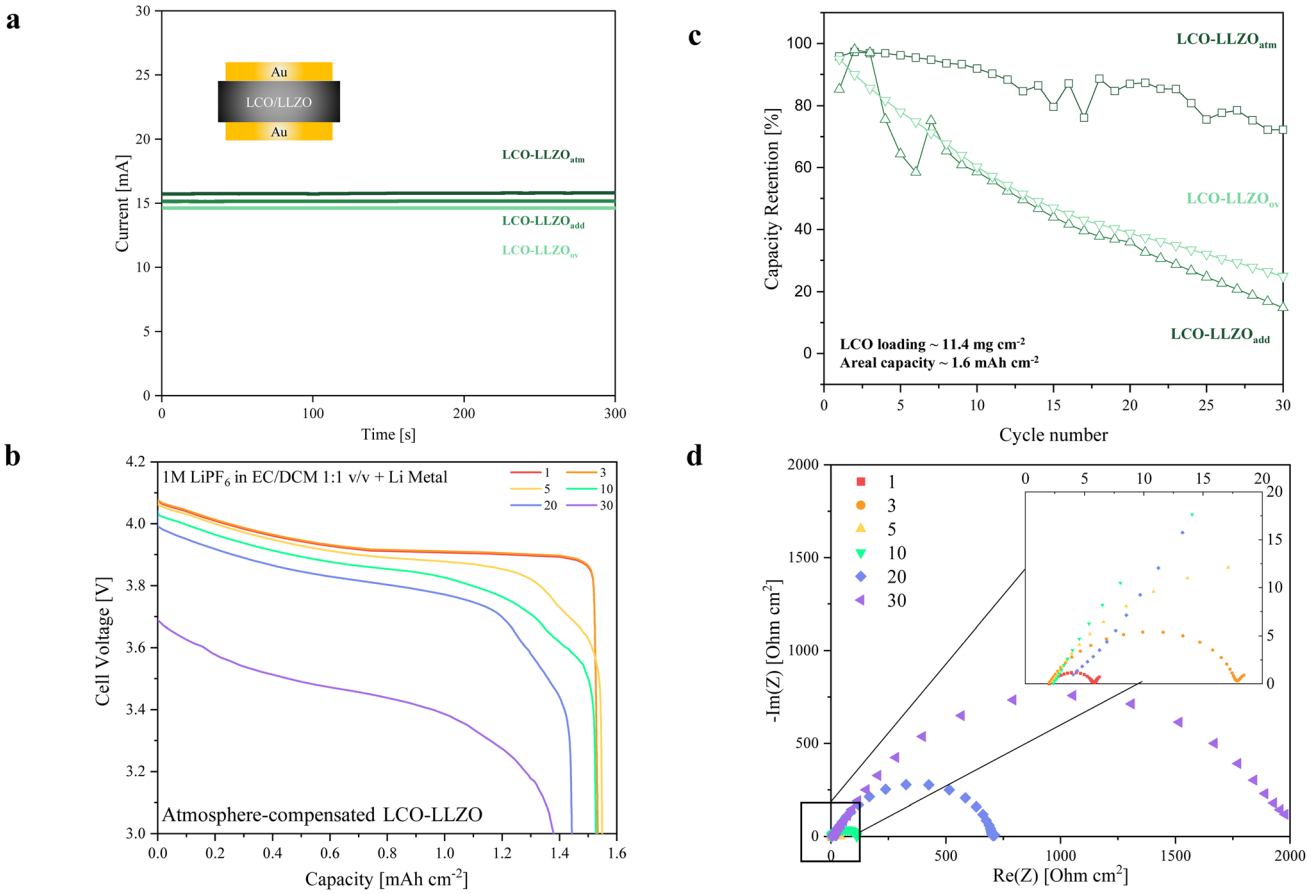

Fig. 6 Electrochemical evaluation of composite cathodes. (a) Chronoamperometry measurements of composite cathodes with ion-blocking gold electrodes. (b) Capacity retention over cycle number of the LLZO-LCO cathode (c) cell voltage over discharge capacity plot for LCO-LLZO$_{atm}$ cathode. (d) Nyquist plots of the LCO-LLZO$_{atm}$ cathode for 30 cycles.

Additional complications such as poor wetting, high and drifting interfacial resistance, and possible Li plating further obscure the intrinsic transport behavior. To overcome these issues, buffered lithium reservoirs (*e.g.*, Li–In alloys) are often employed as alternative, chemically compatible electrodes to define μ_{Li} while minimizing interfacial reactivity – an approach to be explored in ongoing work beyond the present study.

Subsequently, the cathode membranes were evaluated in composite cathode|liquid electrolyte|Li metal hybrid battery cells to assess electrochemical performance. After weighing and with a 50 wt% active material content (LLZO to LCO mass ratio of 1 : 1; an LCO loading of ≈11.4 mg cm^{-2}), we calculated the areal capacity of the cathodes at ≈1.6 mAh cm^{-2}, assuming a practical capacity of 140 mAh g^{-1} for the LCO. The high density of the cathodes limits penetration of liquid electrolyte into the cathode, making them well suited to evaluate the cathode performance. The LCO-LLZO$_{atm}$ full-cell delivered a first discharge capacity of 1.55 mAh cm^{-2} or 136 mAh g_{CAM}^{-1} measured at a current density of 0.25 mA cm^{-2} (≈C-rate of C/6) (Fig. 6b), demonstrating near-complete utilization of the cathode active material. Overall, tested cathode membranes deliver initial discharge capacities exceeding 90% of their theoretical value (SI 12). Cathode active material loadings and capacities are compared in SI 14. Initial impedance spectra showed a total resistance of ≈5.8 Ω cm^2 for the LCO-LLZO$_{atm}$ cathode, showcasing a reduction from ≈20 Ω cm^2 as reported previously in our pellet study.[23] However, upon subsequent cycling, a progressive capacity fade was accompanied by an increase in impedance (Fig. 6c and d). Among the tested cathodes, the LCO-LLZO$_{atm}$ cathode showed the most stable performance, retaining 66% of its capacity after 30 cycles (Fig. 6d). In contrast, the LCO-LLZO$_{add}$ cathode experienced an early capacity loss within the first 5 cycles and then degraded more rapidly, reaching only 15% retention after 30 cycles. The LCO-LLZO$_{ov}$ cathode performed slightly better, maintaining 25% retention after 30 cycles. This modest improvement is likely associated with reduced initial porosity, which may delay the onset of crack formation and propagation.

Upon cycling, the composite cathodes exhibited microcracks both within the bulk and at the interfaces (SI 13). Post-mortem SEM cross-sections of all three cathodes reveal qualitatively similar microcrack morphologies, consistent with chemo-mechanical strain of LCO during repeated cycling, however, a quantitative crack-density/length analysis was not performed. These cracks likely originate from the repeated volume changes of LCO during lithiation and delithiation. While the cracking

patterns are broadly comparable, we attribute the difference in cycling stability primarily to the as-sintered microstructures, where the additive-derived cathodes exhibit higher residual porosity which can serve as stress concentrators and crack-initiation sites, whereas atmosphere samples have higher initial density. Although a lower upper cut-off voltage could improve stability by reducing the SOC swing, we selected 4.1 V to demonstrate mAh-class areal capacity under a practically relevant high-energy condition; the incremental strain from 4.0 to 4.1 V is expected to be modest compared with microstructure-driven effects like porosity and interfacial integrity.[48] In future work, strain accommodation will be addressed primarily through composite mechanics and targeted microstructural design. In the present architecture, LCO particles are mechanically constrained by the continuous and stiff LLZO framework, which limits unconstrained particle expansion and instead concentrates deformation near the interfaces. Consequently, strategies that improve interfacial integrity become particularly important. In addition, reducing LCO particle/grain size and tailoring particle morphology are expected to mitigate stress buildup. Diffusion-induced stress analyses generally predict that the maximum mechanical stress increases with increasing grain size;[49] therefore, shifting from the present 3–5 μm grains toward a sub-micron regime should substantially reduce crack-driving forces under otherwise comparable conditions. This consideration will guide the next generation of monolithic cathode designs.

Raman spectra of cycled cathode particles show features assignable to Co_3O_4, suggesting that local oxygen release and partial transition of $Li_{1-x}CoO_2$ to lower-valence cobalt oxides may occur in isolated regions. These microcracks and possible local phase changes could disrupt continuous ion- and electron-transport pathways, increase local resistance, and induce particle-level state-of-charge heterogeneity. Locally over-delithiated LCO domains may therefore undergo additional structure degradation through oxygen loss,[47] although the precise mechanism requires further investigations.[50,51]

On the anode side, degradation can also occur through reactions between the liquid electrolyte, Li metal, and LLZO, leading to the formation of solid-electrolyte interphases (SEI)[52] that consume cyclable lithium and contribute to the initial irreversible capacity loss. During continuous plating and stripping, the Li surface morphology evolves dynamically, repeatedly exposing fresh surfaces and promoting further SEI formation. Detached dendritic fragments may further reduce accessible lithium. However, given the large lithium reservoir in our cell (~22 mAh), these effects are expected to be minor, and the LCO phase should remain fully lithiated during discharge. Simultaneously, carbonate by-products such as Li_2CO_3 may accumulate at the LLZO/LE interface, gradually etching the garnet surface chemically and diminishing its ionic conductivity.[53] Collectively, these cathode- and anode-side degradation processes introduce irreversible charge consumption and increasing polarization, which is consistent with our observed coulombic efficiency below unity and its deterioration upon cycling (SI 12).

Nonetheless, prior studies have shown that LCO-LLZO composite cathodes can maintain mechanical integrity even after prolonged cycling at higher voltages than those employed here,[54] provided that a highly dense and well-bonded microstructure is achieved. This suggests that the cracking observed in our samples likely arises from insufficient mechanical robustness rather than intrinsic interfacial incompatibility. Hence, further optimization toward enhanced microstructural density and refined grain size distribution will be crucial to improve both the mechanical strength and the long-term electrochemical stability of the composite cathode.

Conclusion

Co-firing of oxide-based composite cathodes is a long-standing bottleneck for solid-state batteries: lithium loss at high temperatures drives parasitic interphases and porosity, which in turn limit the achievable capacity and scale-up of solid-state batteries. By establishing solid-phase lithium compensation routes during co-firing, we address this materials-processing gap and outline practical paths toward manufacturable membranes.

Using $LiCoO_2$ – LLZO as a model system, we introduce two solid-phase compensation routes – Li-containing precursor additives and an overlithiated LLZO catholyte – that suppress $LaCoO_3$-type interphases and enable fully dense, secondary-phase-free microstructures at 1050 °C. Both routes are reproducibly implemented in 100 μm free-standing membranes *via* tape casting, delivering low-resistance hybrid batteries with discharge capacities of up to 1.49 mAh cm^{-2} at C/6. Within the context of co-sintered garnet-based oxide cathodes, this places our membranes among the few reporting both dense, interphase-controlled microstructures and mAh-class areal capacities at practical thickness – without relying on non-scalable equipment or gas-phase lithiation.

The key impact is twofold. Fundamentally, we quantify and mitigate lithium loss during co-firing, clarifying the role of lithium chemical potential in densification and interphase chemistry. Technologically, we provide a scalable, tape castable process window and two interchangeable levers that can be potentially generalized to other oxide cathodes beyond LCO. Together, these advances tighten processing-structure–property links for garnet composites and move fully ceramic, industry-relevant solid-state cathodes closer to deployment.

Experimental section

Component manufacturing

Synthesis of LLZO powders. Cubic-phase Ta- and Al-doped $Li_{6.45}Al_{0.05}La_3Zr_{1.6}Ta_{0.4}O_{12}$ (LLZO) powders were synthesized *via* a solid-state reaction at a batch size of 100 g. Precursor powders with stoichiometric amounts of anhydrous lithium hydroxide (Thermo Scientific, 99.995%), lanthanum(III) hydroxide (Thermo Scientific, 99.95%), zirconium(IV) oxide (Thermo Scientific, 99.7%), aluminum oxide (Thermo Scientific, 99%), and tantalum(V) oxide (Thermo Scientific, 99.85%) were prepared with an excess of 15 wt% LiOH. The powders were then homogeneously mixed in a zirconia (ZrO_2) jar with ZrO_2 milling beads (Retsch) and isopropanol (VWR Chemicals,

99.8%) using a planetary ball mill (Retsch, PM100). The powders were dried and pressed uniaxially into pellets before calcination in ambient air at 750 °C for 2 h. After calcination the green bodies were pre-sintered with an isothermal hold at 1050 °C for 5 h to assure phase stabilization of the cubic phase. Subsequently, the pellets were ground in a mortar and ball milled for 24 h at 300 rpm. After drying, powders were sieved for 30 min in a 400-mesh test sieve to assure monodisperse particle distributions. Powders were then stored in an argon-filled glovebox ($[H_2O]$ < 0.1 ppm, $[O_2]$ < 0.1 ppm). Overlithiated LLZO powders were synthesized accordingly but with higher lithium contents, aiming for a nominal composition of $Li_{7.75}Al_{0.05}La_3Zr_{1.6}Ta_{0.4}O_{12}$. For readability, we refer to this material as $LLZO_{Ov}$ throughout the manuscript and "LLZO" denotes the Ta/Al-stabilized garnet with its minor Al addition as defined here. For reaction equations and discussions, we also neglect the aluminum for simplicity. The Ta/Al-stabilized LLZO composition was selected because it can be densified at 1050 °C while retaining high room-temperature ionic conductivity; in our previous work, dense pellets sintered at 1050 °C reached 0.75 mS cm^{-1}.[23] This compatibility with the thermal budget is critical for future one-step co-firing of separator and composite cathode layers.

Fabrication of LCO-LLZO pellets. The synthesized LLZO or overlithiated LLZO was dry mixed with commercial $LiCoO_2$ (Thermo Scientific, 99,5%) in a ratio of 50 : 50 wt% for 5 min in a planetary mixer (Thinky) at 500 rpm with ZrO_2 milling media to break up agglomerates. Samples for LiOH additive were mixed with 1 wt%, respectively. The obtained powder mixture was pressed into 13 mm pellets with 5 MPa and sintered inside an MgO crucible in a tube furnace in oxygen atmosphere (50 cm^3 h^{-1}) at 1050 °C for 2 h with heating and cooling rates of 5 K min^{-1}. A Li_2O-rich atmosphere was created using a closed-lid crucible with 0.1 g of non-touching LiOH bed powder on the bottom and MgO plates as platforms for the cathode pellets, as described in our previous work.[23] As-sintered pellets were polished using SiC papers, ending with 4000 grit size. Pellets for grain size distribution measurements were then thermally etched in oxygen atmosphere at 900 °C for 1 h.

Fabrication of LCO-LLZO tapes. SE and CAM powders, as well as 2 wt% LiOH for additive samples, were suspended in a slurry matrix consisting of isopropanol and toluene as solvents, menhaden fish oil as dispersant, benzyl butyl phthalate as plasticizer and polyvinyl butyral as binder. ZrO_2 balls were used as mixing media. All components were mixed in a Thinky ARE-250 planetary centrifugal mixer at 1500 rpm to partially suspend the powder in the slurry matrix. The suspension was sonicated to break up agglomerates and finally mixed again in the centrifugal mixer for 3 min to obtain homogenous slurries. After mixing, the slurries were cast onto a Mylar foil using a 200 μm doctor blade. The tapes were dried at room temperature for at least 20 minutes and then removed from the Mylar foil. Tapes were stacked for desired thickness and laminated twice for 5 min at 65 °C and 60 MPa with a laminator (MTI Corporation). After cooling down, circles were punched from the laminated green tapes. The punched-out green tapes were co-fired in a magnesia crucible with a lid in a tube furnace in oxygen atmosphere, parallel to the pellet samples. For a non-contact bed powder approach, the green tapes were sintered as described in our previous work. However, for all tapes we used setter plates and spacers. To achieve flat tapes, green tapes were placed between two magnesia setter plates. To avoid applying weight on top of the tapes, approximately 10 μm-thicker magnesia spacers than the tapes were inserted between the setter plates. This setup reduced the load on the tapes while still limiting available space, effectively preventing warping.

Fabrication of polyethylene oxide. For the preparation of PEO as electrolyte, 0.33 g lithium bis(trifluoromethanesulfonyl) imide was dissolved in 10 mL acetonitrile. While stirring, 1 g of PEO was added to achieve an ethylene oxide to Li^+ ratio of 20 : 1. To fully dissolve the PEO, the solution was stirred for 3 h, and the resulting homogeneous solution was drop-cast into a PTFE evaporation dish. After drying under vacuum at room temperature, the PEO film was peeled off the dish and punched out to match the dimension of the LLZO/LCO composite cathode tape.

Cell assembly. Swagelok cells were assembled in an argon-filled glove box using the prepared secondary-phase free tapes as cathode, lithium metal disks as anode, a Celgard separator and 1 M of $LiPF_6$ dissolved in ethylene carbonate (EC)/dimethyl carbonate (DMC) (1 : 1 in mass) as electrolyte. Before assembly, the tapes were mechanically polished to a thickness of 80 microns with SiC paper, ending with 4000 grit size. One side of the tape was sputtered with a 50 nm gold layer acting as a current collector. Before testing, the cell was rested for 24 h at room temperature.

Characterization

Dilatometry. Composite cathode pellet-type samples were pressed into 6 mm diameter and 12 mm long rods. Using a Linseis DIL L76 and an alumina measuring system, the samples were tested with a constant heating rate of 5 °C min^{-1} until 1100 °C continuously flushed with 50 mL min^{-1} oxygen. To limit contamination, samples were sandwiched between alumina spacers with a force of 50 mN so that the pushrod and backstop are not in contact.

Raman spectroscopy. Raman spectra were collected using a confocal WITec alpha300 R Raman microscope (WITec, Germany) with a 532 nm excitation wavelength. The measurements were performed in air. For the mapping, an area of 25 by 25 μm was selected to perform a stepwise raster, scanning 25 lines with each 25 points per line, resulting in 225 spectra per map. Averaged spectra were computed from all 225 spectra per map. Subsequently, we performed integration over specified peak ranges identified within the Raman spectra. The integration focuses on CCD counts, and the results are presented relative to the integrated count mass.

Powder X-ray diffraction (p-XRD). P-XRD measurements were conducted on ground samples which were sealed inside 0.3 mm glass capillaries. P-XRD measurements were performed at room temperature on a STOE Stadi P diffractometer equipped with a Ge (111) monochromator for Mo $K_{\alpha 1}$ radiation (λ = 0.7093 Å) and a Dectris MYTHEN DCS 1K solid-state detector.

The raw powder data were processed with the software package WinXPOW. Profile fits were executed with the least-squares method implemented in the EXPO2014 software.[55–57] Background contribution was determined using a shifted Cebyshev function and non-structural parameters were refined with the Le Bail method. Note that the low-angle reflection may appear mildly asymmetric due to axial-divergence-related instrumental line-shape effects in conventional geometries, rather than indicating an additional crystalline phase.[58]

Scanning electron microscopy (SEM). SEM images were acquired using a Hitachi TM400Plus tabletop scanning electron microscope at 15 kV with a backscattered electron detector. An in-lens SE detector was used for the top view images of LCO particles, and a BED-C detector was used for the cross-sectional SEM images of the LLZO and LLZO/LCO tapes. Conductive carbon tape was used to tape the samples to the sample holder and ensure sufficient electronic conductivity during imaging. Grain size distribution measurements were carried out utilizing ImageJ.

Inductively coupled plasma optical emission spectrometry (ICP-OES). ICP-OES measurements were collected using a 5800 ICP-OES instrument from Agilent Technologies. Powdered samples were dissolved in *aqua regia* – 3 : 1 molar ratio of HCl (Sigma-Aldrich, 30%) to HNO_3 (Sigma-Aldrich, 70%) – and three aliquots of each sample solution were diluted in Millipore water prior to the measurement. The device was calibrated using four multi-element calibration solutions prepared from ICP standard solutions (Sigma-Aldrich) containing the elements Li, La, Ta and Zr (Sigma-Aldrich) in stoichiometric amounts as expected for LLZO. *Aqua regia* was added to each calibration solution and to the blank solution in amounts matching the amount contained in the sample solution to ensure an identical matrix background. Measurements were performed in radial geometry and the following wavelengths were evaluated for the respective elements: 670 nm for lithium, 263 nm for tantalum, 333 nm for lanthanum, and 343 nm for zirconium. Li-contents were calculated by normalization of the obtained Li- and La-concentrations to stoichiometric La-content of 3.0 pfu.

Optical profilometry. A 3D profilometer (VK3100, Keyence Corporation, Osaka, Japan) was employed to manually assess the surface topography of each sample. The corresponding analysis software (VR–3000 G2, Keyence Corporation, Japan) was used to determine the arithmetic mean surface roughness (S_a).

Electrochemical impedance spectroscopy (EIS) and battery testing. Electrochemical impedance spectroscopy and cycling of the all-solid-state cathode was conducted at room temperature using a BioLogic VSP-300 potentiostat/galvanostat (Bio-Logic, Knoxville, TN, USA). The samples were then tested in a Swagelok-type cell (Beyond Battery) in a climate chamber at 25 °C, applying frequencies between 7 MHz and 1 Hz with an electrical field perturbation of 10 mV. For electronic blocking conditions, cathode tapes were placed in between the free-standing PEO rested in a split cell at 60 °C for 24 h before testing. For electrochemical cycling, the cells were charged and discharged over a potential range of 3–4.1 V (against lithium) at 0.25 mA cm^{-2} current density (C-rate of C/6) at room temperature. Between every charge and discharge, EIS was measured from 1 MHz to 100 Hz.

Chronoamperometry (CA). 50 nm-thick Au films were deposited on both sides of the cathode tapes by DC-sputtering. With a BioLogic VSP-300, a potential of 100 mV was applied to the gold-sputtered composite cathodes and the current response was measured over two h.

Conflicts of interest

The authors declare that they have no known competing financial interests or personal relationships that could have appeared to influence the work reported in this paper.

Data availability

Supplementary information (SI): supplementary Fig. S1–S14 include SEM images, Raman spectra, XRD data with Rietveld refinements, Raman mapping, impedance analysis, and additional electrochemical cycling results. See DOI: https://doi.org/10.1039/d5ta09479h.

Acknowledgements

The authors gratefully acknowledge the funding from the German Federal Ministry of Education and Research (BMBF). The results presented in this work have been achieved within the project FestBatt2-Oxide (grant number: 03XP0434A). Further, we acknowledge support by the project “Industrialisierbarkeit von Festkörperelektrolytzellen” funded by the Bavarian Ministry of Economic Affairs, Regional Development and Energy.

References

1 T. Kim, W. Song, D.-Y. Son, L. K. Ono and Y. Qi, Lithium-ion batteries: outlook on present, future, and hybridized technologies, *J. Mater. Chem. A*, 2019, **7**, 2942–2964, DOI: 10.1039/C8TA10513H.

2 K. J. Kim, M. Balaish, M. Wadaguchi, L. Kong and J. L. M. Rupp, Solid-State Li–Metal Batteries: Challenges and Horizons of Oxide and Sulfide Solid Electrolytes and Their Interfaces, *Adv. Energy Mater.*, 2021, **11**, 2002689, DOI: 10.1002/aenm.202002689.

3 J. Janek and W. G. Zeier, Challenges in speeding up solid-state battery development, *Nat. Energy*, 2023, **8**, 230–240, DOI: 10.1038/s41560-023-01208-9.

4 T. Schmaltz, F. Hartmann, T. Wicke, L. Weymann, C. Neef and J. Janek, A Roadmap for Solid-State Batteries, *Adv. Energy Mater.*, 2023, **13**, 2301886, DOI: 10.1002/aenm.202301886.

5 M. Balaish, K. J. Kim, H. Chu, Y. Zhu, J. C. Gonzalez-Rosillo, H. Paik, S. Weinmann, Z. D. Hood, J. J. Hinricher, L. J. Miara, *et al.*). Emerging Processing Guidelines for Solid Electrolytes in the Era of Oxide-Based Solid-State Batteries, *Chem. Soc. Rev.*, 2025, **54**, 8925–9007.

6 C. Bauer, S. Burkhardt, N. P. Dasgupta, L. A.-W. Ellingsen, L. L. Gaines, H. Hao, R. Hischier, L. Hu, Y. Huang, J. Janek, *et al.*). Charging sustainable batteries, *Nat Sustainability*, 2022, **5**, 176–178, DOI: 10.1038/s41893-022-00864-1.

7 Y. Ren, T. Danner, A. Moy, M. Finsterbusch, T. Hamann, J. Dippell, T. Fuchs, M. Müller, R. Hoft, A. Weber, *et al.*). Oxide-Based Solid-State Batteries: A Perspective on Composite Cathode Architecture, *Adv. Energy Mater.*, 2023, **13**, 2201939, DOI: 10.1002/aenm.202201939.

8 S. C. Sand, J. L. M. Rupp and B. Yildiz, A critical review on Li-ion transport, chemistry and structure of ceramic–polymer composite electrolytes for solid state batteries, *Chem. Soc. Rev.*, 2025, **54**, 178–200, DOI: 10.1039/D4CS00214H.

9 M. Balaish, J. C. Gonzalez-Rosillo, K. J. Kim, Y. Zhu, Z. D. Hood and J. L. M. Rupp, Processing thin but robust electrolytes for solid-state batteries, *Nat. Energy*, 2021, **6**, 227–239, DOI: 10.1038/s41560-020-00759-5.

10 Y. Zhu, J. C. Gonzalez-Rosillo, M. Balaish, Z. D. Hood, K. J. Kim and J. L. M. Rupp, Lithium-film ceramics for solid-state lithionic devices, *Nat. Rev. Mater.*, 2020, **6**, 313–331, DOI: 10.1038/s41578-020-00261-0.

11 P. Albertus, V. Anandan, C. Ban, N. Balsara, I. Belharouak, J. Buettner-Garrett, Z. Chen, C. Daniel, M. Doeff, N. J. Dudney, *et al.*). Challenges for and Pathways toward Li-Metal-Based All-Solid-State Batteries, *ACS Energy Lett.*, 2021, 1399–1404, DOI: 10.1021/acsenergylett.1c00445.

12 G. T. Hitz, D. W. McOwen, L. Zhang, Z. Ma, Z. Fu, Y. Wen, Y. Gong, J. Dai, T. R. Hamann, L. Hu, *et al.*). High-rate lithium cycling in a scalable trilayer Li-garnet-electrolyte architecture, *Mater. Today*, 2019, **22**, 50–57, DOI: 10.1016/j.mattod.2018.04.004.

13 M. Wang and J. Sakamoto, Correlating the interface resistance and surface adhesion of the Li metal-solid electrolyte interface, *J. Power Sources*, 2018, **377**, 7–11, DOI: 10.1016/j.jpowsour.2017.11.078.

14 E. Kazyak, M. J. Wang, K. Lee, S. Yadavalli, A. J. Sanchez, M. D. Thouless, J. Sakamoto and N. P. Dasgupta, Understanding the electro-chemo-mechanics of Li plating in anode-free solid-state batteries with operando 3D microscopy, *Matter*, 2022, **5**, 3912–3934, DOI: 10.1016/j.matt.2022.07.020.

15 G. V. Alexander, Extreme lithium-metal cycling enabled by a mixed ion- and electron-conducting garnet three-dimensional architecture, *Nat. Mater.*, 2023, **22**, 1136–1143.

16 A. Sharafi, E. Kazyak, A. L. Davis, S. Yu, T. Thompson, D. J. Siegel, N. P. Dasgupta and J. Sakamoto, Surface Chemistry Mechanism of Ultra-Low Interfacial Resistance in the Solid-State Electrolyte $Li_7La_3Zr_2O_{12}$, *Chem. Mater.*, 2017, **29**, 7961–7968, DOI: 10.1021/acs.chemmater.7b03002.

17 A. Gruendl, S. Weinmann, J. Goehmann, J. Landau, M. Lechner, L. Mueller, K. J. Kim, J. L. M. Rupp and M. F. Zaeh, Process strategies for the laser-based surface treatment of garnet-type ceramics used in solid-state batteries, *Opt Laser. Technol.*, 2025, **189**, 113118, DOI: 10.1016/j.optlastec.2025.113118.

18 J. H. Cho, K. Kim, S. Chakravarthy, X. Xiao, J. L. M. Rupp and B. W. Sheldon, An Investigation of Chemo-Mechanical Phenomena and Li Metal Penetration in All-Solid-State Lithium Metal Batteries Using *In Situ* Optical Curvature Measurements, *Adv. Energy Mater.*, 2022, **12**, 2200369, DOI: 10.1002/aenm.202200369.

19 K. J. Kim and J. L. M. Rupp, All ceramic cathode composite design and manufacturing towards low interfacial resistance for garnet-based solid-state lithium batteries, *Energy Environ. Sci.*, 2020, **13**, 4930–4945, DOI: 10.1039/D0EE02062A.

20 W. S. Scheld, K. Kim, C. Schwab, A. C. Moy, S. Jiang, M. Mann, C. Dellen, Y. J. Sohn, S. Lobe, M. Ihrig, *et al.*). The Riddle of Dark LLZO: Cobalt Diffusion in Garnet Separators of Solid-State Lithium Batteries, *Adv. Funct. Mater.*, 2023, 2302939, DOI: 10.1002/adfm.202302939.

21 H. Yamada, T. Ito, T. Nakamura, R. Bekarevich, K. Mitsuishi, S. P. Kammampata and V. Thangadurai, High Cathode Loading and Low-Temperature Operating Garnet-Based All-Solid-State Lithium Batteries – Material/Process/Architecture Optimization and Understanding of Cell Failure, *Small*, 2023, **19**, 2301904, DOI: 10.1002/smll.202301904.

22 W. S. Scheld, S. Lobe, C. Dellen, M. Ihrig, G. Häuschen, L. C. Hoff, M. Finsterbusch, S. Uhlenbruck, O. Guillon and D. Fattakhova-Rohlfing, Rapid thermal processing of garnet-based composite cathodes, *J. Power Sources*, 2022, **545**, 231872, DOI: 10.1016/j.jpowsour.2022.231872.

23 S. Weinmann, H. Gobena, L. Quincke, J. J. Hinricher, S. Merk, H. Chu, T. Prein, J. L. M. Rupp and K. J. Kim, Stabilizing Interfaces of All-Ceramic Composite Cathodes for Li-Garnet Batteries, *Adv. Energy Mater.*, 2025, **15**, 2502280.

24 L. Li, J. Andrews, R. Mitchell, D. Button, D. C. Sinclair and I. M. Reaney, Aqueous Cold Sintering of Li-Based Compounds, *ACS Appl. Mater. Interfaces*, 2023, **15**, 20228–20239, DOI: 10.1021/acsami.3c00392.

25 W. S. Scheld, J. N. Ebert, M. Scherer, L. Fulanovic, L. Porz, C. Dellen, M. Ihrig, S. Uhlenbruck, M. Finsterbusch, O. Guillon, *et al.*). Blacklight sintering of garnet-based composite cathodes, *J. Eur. Ceram. Soc.*, 2024, **44**, 3039–3048, DOI: 10.1016/j.jeurceramsoc.2023.12.040.

26 H.-J. Kim, H. Shin, J. H. Kim and S.-W. Baek, Interfacial stability of gas-controlled LCO:Ta-LLZO cathodes composite for all-solid-state batteries, *J. Alloys Compd.*, 2025, **1027**, 180616, DOI: 10.1016/j.jallcom.2025.180616.

27 R. Ye, M. Ihrig, E. Figgemeier, D. Fattakhova-Rohlfing and M. Finsterbusch, Aqueous Processing of $LiCoO_2$–$Li_{6.6}La_3Zr_{1.6}Ta_{0.4}O_{12}$ Composite Cathode for High-Capacity Solid-State Lithium Batteries, *ACS Sustainable Chem. Eng.*, 2023, 2c07556, DOI: 10.1021/acssuschemeng.2c07556.

28 S. Weinmann, L. Quincke, L. Winkler, J. J. Hinricher, F. Kurnia, K. J. Kim and J. L. M. Rupp, Sustainable Functional Ceramics, *Nat. Nanotechnol.*, 2025, **20**, 1729–1745.

29 L. N. Dinh, W. McLean Ii, M. A. Schildbach, J. D. LeMay, W. J. Siekhaus and M. Balooch, The nature and effects of

the thermal stability of lithium hydroxide, *J. Nucl. Mater.*, 2003, **317**, 175–188, DOI: 10.1016/S0022-3115(03)00084-9.

30 J. M. Kiat, G. Boemare, B. Rieu and D. Aymes, Structural evolution of LiOH: evidence of a solid–solid transformation toward Li2O close to the melting temperature, *Solid State Commun.*, 1998, **108**, 241–245, DOI: 10.1016/S0038-1098(98)00346-9.

31 F. Tietz, T. Wegener, M. T. Gerhards, M. Giarola and G. Mariotto, Synthesis and Raman micro-spectroscopy investigation of Li7La3Zr2O12, *Solid State Ionics*, 2013, **230**, 77–82, DOI: 10.1016/j.ssi.2012.10.021.

32 G. Larraz, A. Orera and M. L. Sanjuán, Cubic phases of garnet-type Li7La3Zr2O12: the role of hydration, *J. Mater. Chem. A*, 2013, **1**, 11419, DOI: 10.1039/c3ta11996c.

33 Y. Zhu, M. Chon, C. V. Thompson and J. L. M. Rupp, Time-Temperature-Transformation (TTT) Diagram of Battery-Grade Li-Garnet Electrolytes for Low-Temperature Sustainable Synthesis, *Angew. Chem.*, 2023, **135**, e202304581, DOI: 10.1002/ange.202304581.

34 T. Gross and C. Hess, Raman diagnostics of LiCoO2 electrodes for lithium-ion batteries, *J. Power Sources*, 2014, **256**, 220–225, DOI: 10.1016/j.jpowsour.2014.01.084.

35 E. Rangasamy, J. Wolfenstine and J. Sakamoto, The role of Al and Li concentration on the formation of cubic garnet solid electrolyte of nominal composition Li7La3Zr2O12, *Solid State Ionics*, 2012, **206**, 28–32, DOI: 10.1016/j.ssi.2011.10.022.

36 S.-K. Jung, H. Gwon, H. Kim, G. Yoon, D. Shin, J. Hong, C. Jung and J.-S. Kim, Unlocking the hidden chemical space in cubic-phase garnet solid electrolyte for efficient quasi-all-solid-state lithium batteries, *Nat. Commun.*, 2022, **13**, 7638, DOI: 10.1038/s41467-022-35287-1.

37 G. G. Amatucci, J. M. Tarascon and L. C. Klein, CoO2, The End Member of the Li x CoO2 Solid Solution, *J. Electrochem. Soc.*, 1996, **143**, 1114–1123, DOI: 10.1149/1.1836594.

38 F. Khatun, M. A. Gafur, M. S. Ali, M. S. Islam and M. A. R. Sarker, Impact of Lithium Composition on Structural, Electronic and Optical Properties of Lithium Cobaltite Prepared by Solid-state Reaction, *J. Sci. Res.*, 2014, **6**, 217–231, DOI: 10.3329/jsr.v6i2.17900.

39 J. Tan, Z. Wang, G. Li, H. Hu, J. Li, R. Han and D. Zhang, Electrochemically Driven Phase Transition in LiCoO2 Cathode, *Materials*, 2021, **14**, 242, DOI: 10.3390/ma14020242.

40 A. G. Squires, D. O. Scanlon and B. J. Morgan, Native Defects and Their Doping Response in the Lithium Solid Electrolyte Li_7 La_3 Zr_2 O_{12}, *Chem. Mater.*, 2020, **32**, 1876–1886, DOI: 10.1021/acs.chemmater.9b04319.

41 R. A. Jonson, E. Yi, F. Shen and M. C. Tucker, Optimization of Tape Casting for Fabrication of Li $_{6.25}$ Al $_{0.25}$ La $_3$ Zr $_2$ O $_{12}$ Sheets, *Energy Fuels*, 2021, **35**, 8982–8990, DOI: 10.1021/acs.energyfuels.1c00566.

42 N. Janani, S. Ramakumar, S. Kannan and R. Murugan, Optimization of Lithium Content and Sintering Aid for Maximized Li^+ Conductivity and Density in Ta-Doped Li_7 La_3 Zr_2 O_{12}, *J. Am. Ceram. Soc.*, 2015, **98**, 2039–2046, DOI: 10.1111/jace.13578.

43 L. J. Miara, S. P. Ong, Y. Mo, W. D. Richards, Y. Park, J.-M. Lee, H. S. Lee and G. Ceder, Effect of Rb and Ta Doping on the Ionic Conductivity and Stability of the Garnet Li 7+2 x – y (La 3– x Rb x)(Zr 2– y Ta y)O12 ($0 \leq x \leq 0.375$, $0 \leq y \leq 1$) Superionic Conductor: A First Principles Investigation, *Chem. Mater.*, 2013, **25**, 3048–3055, DOI: 10.1021/cm401232r.

44 X. Huang, Y. Lu, Z. Song, T. Xiu, M. E. Badding and Z. Wen, Preparation of dense Ta-LLZO/MgO composite Li-ion solid electrolyte: Sintering, microstructure, performance and the role of MgO, *J. Energy Chem.*, 2019, **39**, 8–16, DOI: 10.1016/j.jechem.2019.01.013.

45 B. Wu, R. Yi, Y. Xu, P. Gao, Y. Bi, L. Novák, Z. Liu, E. Hu, N. Wang, J. Rijssenbeek, *et al.*). Unusual Li2O sublimation promotes single-crystal growth and sintering, *Nat. Energy*, 2025, **10**, 605–615, DOI: 10.1038/s41560-025-01738-4.

46 X. Huang, Y. Lu, Z. Song, K. Rui, Q. Wang, T. Xiu, M. E. Badding and Z. Wen, Manipulating Li2O atmosphere for sintering dense Li7La3Zr2O12 solid electrolyte, *Energy Storage Mater.*, 2019, **22**, 207–217, DOI: 10.1016/j.ensm.2019.01.018.

47 I. Riess, Review of the limitation of the Hebb-Wagner polarization method for measuring partial conductivities in mixed ionic electronic conductors, *Solid State Ionics*, 1996, 221–232.

48 J. N. Reimers and J. R. Dahn, Electrochemical and *In Situ* X-Ray Diffraction Studies of Lithium Intercalation in Li x CoO2, *J. Electrochem. Soc.*, 1992, **139**, 2091–2097, DOI: 10.1149/1.2221184.

49 J. Christensen and J. Newman, Stress generation and fracture in lithium insertion materials, *J. Solid State Electrochem.*, 2006, **10**, 293–319, DOI: 10.1007/s10008-006-0095-1.

50 J. Seok, W. Lee, H. Lee, S. Park, C. Chung, S. Hwang and W.-S. Yoon, Aging Mechanisms of Lithium-ion Batteries, *J. Electrochem. Sci. Technol.*, 2024, **15**, 51–66, DOI: 10.33961/jecst.2023.00724.

51 R. Zhan, X. Wang, Z. Chen, Z. W. Seh, L. Wang and Y. Sun, Promises and Challenges of the Practical Implementation of Prelithiation in Lithium-Ion Batteries, *Adv. Energy Mater.*, 2021, **11**, 2101565, DOI: 10.1002/aenm.202101565.

52 D. Lu, Y. Shao, T. Lozano, W. D. Bennett, G. L. Graff, B. Polzin, J. Zhang, M. H. Engelhard, N. T. Saenz, W. A. Henderson, *et al.*). Failure Mechanism for Fast-Charged Lithium Metal Batteries with Liquid Electrolytes, *Adv. Energy Mater.*, 2015, **5**, 1400993, DOI: 10.1002/aenm.201400993.

53 A. Gupta, E. Kazyak, N. P. Dasgupta and J. Sakamoto, Electrochemical and Surface Chemistry Analysis of Lithium Lanthanum Zirconium Tantalum Oxide (LLZTO)/Liquid Electrolyte (LE) Interfaces, *J. Power Sources*, 2020, **474**, 228598, DOI: 10.1016/j.jpowsour.2020.228598.

54 M. Ihrig, M. Finsterbusch, A. M. Laptev, C. Tu, N. T. T. Tran, C. Lin, L.-Y. Kuo, R. Ye, Y. J. Sohn, P. Kaghazchi, *et al.*). Study of LiCoO 2/Li 7 La 3 Zr 2 O 12 :Ta Interface Degradation in All-Solid-State Lithium Batteries, *ACS Appl. Mater.*

Interfaces, 2022, **14**, 11288–11299, DOI: 10.1021/acsami.1c22246.

55 A. Altomare, M. C. Burla, M. Camalli, B. Carrozzini, G. L. Cascarano, C. Giacovazzo, A. Guagliardi, A. G. G. Moliterni, G. Polidori and R. Rizzi, EXPO: a program for full powder pattern decomposition and crystal structure solution, *J. Appl. Crystallogr.*, 1999, **32**, 339–340, DOI: 10.1107/s0021889898007729.

56 A. Altomare, M. Camalli, C. Cuocci, C. Giacovazzo, A. Moliterni and R. Rizzi, EXPO2009: structure solution by powder data in direct and reciprocal space, *J. Appl. Crystallogr.*, 2009, **42**, 1197–1202, DOI: 10.1107/s0021889809042915.

57 H. M. Rietveld, A profile refinement method for nuclear and magnetic structures, *J. Appl. Crystallogr.*, 1969, **2**, 65–71, DOI: 10.1107/s0021889869006558.

58 R. W. Cheary and A. A. Coelho, Axial Divergence in a Conventional X-ray Powder Diffractometer. II. Realization and Evaluation in a Fundamental-Parameter Profile Fitting Procedure, *J. Appl. Crystallogr.*, 1998, **31**, 862–868, DOI: 10.1107/S0021889898006888.